

# HSR-KAN: Efficient Hyperspectral Image Super-Resolution via Kolmogorov-Arnold Networks

Baisong Li<sup>1,2</sup>, Xingwang Wang<sup>1,2\*</sup>, Haixiao Xu<sup>1,2</sup>

<sup>1</sup>College of Computer Science and Technology, Jilin University

<sup>2</sup>Key Laboratory of Symbolic Computation and Knowledge Engineering of Ministry of Education, Jilin University

lbs23@mails.jlu.edu.cn, {xww, haixiao}@jlu.edu.cn

## Abstract

Hyperspectral images (HSIs) have great potential in various visual tasks due to their rich spectral information. However, obtaining high-resolution hyperspectral images remains challenging due to limitations of physical imaging. Inspired by *Kolmogorov-Arnold Networks* (KANs), we propose an efficient HSI super-resolution (HSI-SR) model to fuse a low-resolution HSI (LR-HSI) and a high-resolution multispectral image (HR-MSI), yielding a high-resolution HSI (HR-HSI). To achieve the effective integration of spatial information from HR-MSI, we design a fusion module based on KANs, called KAN-Fusion. Further inspired by the channel attention mechanism, we design a spectral channel attention module called *KAN Channel Attention Block* (KAN-CAB) for post-fusion feature extraction. As a channel attention module integrated with KANs, KAN-CAB not only enhances the fine-grained adjustment ability of deep networks, enabling networks to accurately simulate details of spectral sequences and spatial textures, but also effectively avoid *Curse of Dimensionality* (COD). Extensive experiments show that, compared to current state-of-the-art (SOTA) HSI-SR methods, proposed HSR-KAN achieves the best performance in terms of both qualitative and quantitative assessments. Our code is available at: <https://github.com/Baisongm-Li/HSR-KAN>.

## Introduction

Hyperspectral images (HSIs) have numerous spectral bands that provide more accurate information than traditional RGB images. Due to this capability, HSIs hold a pivotal role across various domains of computer vision, encompassing tasks such as image classification (Chen et al. 2023), scene segmentation (Ren et al. 2024), and object tracking (Islam et al. 2024).

Over the past several decades, numerous hyperspectral image super-resolution (HSI-SR) methods have been proposed, generally categorized into four types: Bayesian inference-based (Akhtar, Shafait, and Mian 2015; Wei et al. 2014), matrix decomposition-based (Borsoi, Imbiriba, and Bermudez 2018), tensor-based (Li et al. 2018), and deep learning (DL)-based methods (Hu et al. 2022; Hu, Huang, and Deng 2021; Wu et al. 2023). Bayesian inference-based methods may lack flexibility when dealing with different structures and characteristics of hyperspectral images. Their

effectiveness can be influenced by the distribution of input data and specific prior assumptions, which may result in suboptimal performance across various practical scenarios. Matrix decomposition-based methods typically reshape hyperspectral images into two-dimensional matrices, overlooking their original three-dimensional structure. This oversight can impose limitations when attempting to learn complex relationships between spatial and spectral dimensions. Tensor-based methods involve decomposing and reconstructing high-order tensors, requiring substantial computational resources and complex mathematical operations. This high computational cost is particularly evident when processing large-scale hyperspectral data. Furthermore, traditional methods mentioned above may exhibit limited generalization when handling different types or structures of HSIs, making it challenging to effectively adapt and extend to new datasets or scenarios.

In recent years, a large number of DL-based methods have emerged. Compared to traditional approaches, DL-based methods do not require extensive manual priors and can directly extract features from HSIs for modeling. SR models based on Convolutional Neural Networks (CNNs) (Dong et al. 2016; Hu et al. 2022) initially achieve remarkable results in various SR tasks. Subsequently, Transformer-based models (Hu, Huang, and Deng 2021) make significant progress in HSR due to their powerful sequence modeling capabilities. Additionally, generative models have also been developed in parallel, with models based on Generative Adversarial Networks (GANs) (Ledig et al. 2017; Goodfellow et al. 2020) widely applied in SR for their ability to generate more realistic and intricate high-frequency details. Research into Diffusion-based methods (Wu et al. 2023; Ho, Jain, and Abbeel 2020) is also advancing, particularly for their better detail generation and training stability compared to GAN models.

Despite the aforementioned deep learning methods integrating multilayer perceptrons (MLPs), convolutional neural networks (CNNs), and Transformer architectures, which have introduced a series of innovative designs and significant performance improvements, their core modeling strategy is fundamentally still limited by the constraints of traditional linear modeling paradigms. Specifically, linear deep networks struggle to achieve an optimal balance between computational efficiency and image generation quality when

\*Corresponding Author

dealing with high-dimensional spectral images (Donoho et al. 2000).

Recently, inspired by the Kolmogorov-Arnold representation theorem (Kolmogorov 1957; Tikhomirov 1991), Kolmogorov-Arnold Networks (KANs) (Liu et al. 2024) have been introduced as an innovative computational core. By replacing linear weights at the network’s edges with learnable univariate functions based on b-splines. By incorporating spline functions, neural networks are enabled to achieve a more fine-grained adjustment of spectral features with fewer parameters. Nonetheless, spline functions themselves struggle to escape the constraints of the *Curse Of Dimensionality* (COD) (Sprecher and Draghici 2002; Köppen 2002). The groundbreaking contribution of HSR-KAN lies in its ingenious integration of KANs, MLPs and CNNs, creating a HSI-SR network that strikes an excellent balance between computational efficiency and the quality of image generation.

In this paper, we integrate KANs, MLPs, and CNNs to form a new neural network called HSR-KAN. Our starting point is to meticulously design an effective network structure that leverages strengths of each computational core. While circumventing COD, we strive for optimal balance between model computational efficiency and the quality of image generation. Taking into account fine-grained control ability of spline functions for sequence adjustment, we use three KAN layers in a series of linear transformations as fusion module (called KAN-Fusion) to efficiently fuse LR-HSI and HR-MSI. To avoid the potential COD that may arise from the simplistic stacking of KAN layers, we draw inspiration from SENet (Hu et al. 2019), propose a new attention module called *KAN Channel Attention Block* (KAN-CAB), which uses KAN layers only for adjusting the attention weight of spectral channels. KAN-CAB achieves precise spectral feature adjustment for post-fusion spectral feature with fewer parameters. In summary, HSR-KAN not only efficiently leverages the advantages of KAN but also cleverly avoids the problem of COD. The main contributions of this work are summarized as follows:

1. We propose a module for fusing LR-HSI and HR-MSI called KAN-Fusion. KAN-Fusion can finely fuse spectral sequence features with spatial texture features due to the introduction of KAN.
2. Our proposed KAN-CAB module models the fused spectral features, and through the design of the channel attention structure, it exploits the advantages of KAN while avoiding the COD caused by the spline function.
3. We propose an efficient HSI-SR network called HSR-KAN. HSR-KAN mainly consists of two modules, KAN-Fusion and KAN-CAB, and HSR-KAN effectively integrates the advantages of different computing cores. Extensive experiments demonstrate that HSR-KAN achieves state-of-the-art (SOTA) results and achieves an outstanding balance between computational expense and SR quality.

## Related Works

### Deep Learning-Based HSI-SR

With the development of deep learning, deep neural networks have come to dominate the field of HSI-SR. These approaches treat the HSI-SR task as a nonlinear mapping from LR-HSIs to HR-HSIs, and utilizing gradient descent to fit the mapping network in order to generate optimal HR-HSIs.

CNN is one of the most popular computational cores, is utilized by MHF-Net (Xie et al. 2022) through deep unfolding techniques, creating a multi-layer interpretable super-resolution network based on CNN. SSRNet (Zhang et al. 2021) employs cross-model message insertion (CMMI) to integrate features from LR-HSI and high-resolution multi-spectral HR-HSI base on CNN. HSRnet (Hu et al. 2022) uses LR-HSI of the same scale as HR-MSI, extracting information through spatial attention mechanisms and channel attention mechanisms. With the introduction of Transformer (Vaswani et al. 2017), which powerful attention modeling mechanism has been increasingly applied to HSI-SR tasks. As a pioneer, Fusformer (Hu, Huang, and Deng 2021) achieves remarkable performance through a self-attention mechanism based on spectral channel features. DCTransformer (Ma et al. 2024) captures interactions between different modalities using a directional paired multi-head cross-attention mechanism, efficiently modeling spectral images. With the development of diffusion generative models, diffusion methods have also been introduced into HSR tasks. HSR-Diff (Wu et al. 2023) employs a conditional denoising mode to train the network, generating more Restructured spectral images. However, when dealing with high-dimensional spectral data, these methods often require very deep network structures or a large amount of training data to achieve satisfactory approximation results.

### Kolmogorov-Arnold Networks (KANs)

Due the fine-grained sequence modeling capability, KAN is initially applied to two-dimensional time series prediction. TKAN (Genet and Inzirillo 2024) integrates KAN and LSTM networks for multi-step time series forecasting. However, this approach is not suitable for effectively modeling 3D HSIs because it cannot capture the spatial relationship between spatial pixels effectively. U-KAN (Li et al. 2024) embeds KAN modules into the U-Net network to achieve efficient medical image segmentation. However, for SR tasks, after continuous encoding, U-KAN lead to pixel information loss, and the decoding process will be disrupted by the interference from downsampling low-resolution layers. (Cheon 2024) further validation of the effectiveness of KAN in processing RGB images. However, effectively harnessing KAN networks for modeling hyperspectral images remains a challenge.

## Proposed HSR-KAN Network

### Problem Formulation

The observation model for HR-MSI and LR-HSI is as follows:

$$\mathbf{X} = \mathbf{RZ}, \mathbf{Y} = \mathbf{ZD}, \quad (1)$$

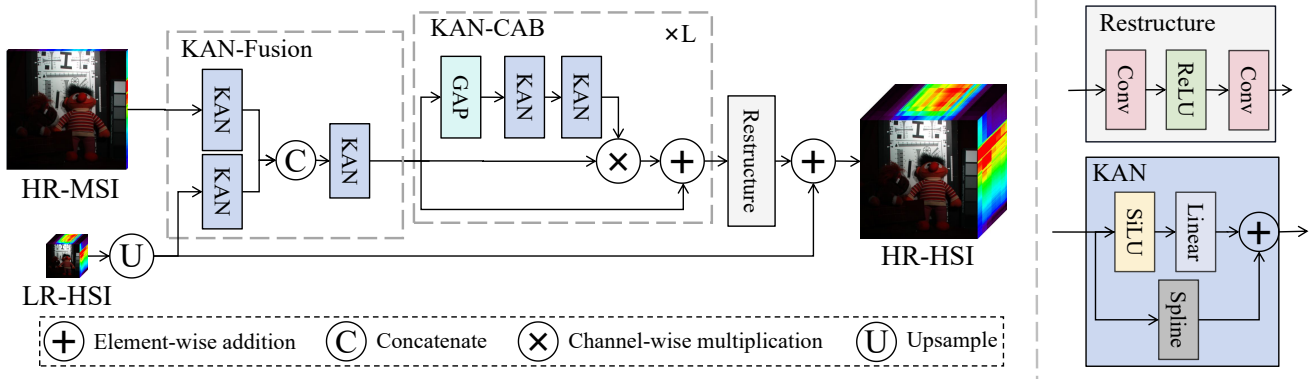


Figure 1: The structure diagram of HSR-KAN. "Conv" denotes a convolutional layer with a  $3 \times 3$  kernel, "ReLU" denotes the *ReLU* activation function, "GAP" denotes the *Global Average Pooling*, "Spline" denotes the *B-spline function*, "SiLU" denotes *SiLU* activation function.

where  $\mathbf{X} \in \mathbb{R}^{c \times H \times W}$  represents HR-MSI,  $\mathbf{Y} \in \mathbb{R}^{C \times h \times w}$  represents LR-HSI, and  $\mathbf{Z} \in \mathbb{R}^{C \times H \times W}$  represents HR-HSI. Here,  $W$  and  $H$  denote the width and height of high-resolution image, respectively, while  $w$  and  $h$  denote the width and height of low-resolution image, respectively.  $C$  and  $c$  represent the number of spectral bands of hyperspectral and multispectral image, respectively.  $D \in \mathbb{R}^{HW \times hw}$  is the spatial response function of LR-HSI, representing the spatial degradation model of HR-HSI.  $R \in \mathbb{R}^{b \times B}$  represents the spectral response function of HR-MSI, describing the spectral degradation model of HR-HSI. HSI-SR can be defined as an inverse problem where a latent  $\mathbf{Z}$  is generated from existing  $\mathbf{X}$  and observed  $\mathbf{Y}$ .

## Architecture Overview

Fig. 1 illustrates the overall framework of HSR-KAN, which consists of three main parts: KAN-Fusion, multi-layer KAN-CAB, and the Restructure module. Initially, LR-HSI and HR-MSI are fused via KAN-Fusion to generate spectral latent features. These features are then input into the multi-layer KAN-CABs for feature extraction. Each layer of KAN-CAB consists of two KANs, forming a SENet (Hu et al. 2019) structure. Finally, the Restructure module through two convolutional layers to adjust the generated latent features into the shape of HR-HSI.

## KAN Layer

In KAN layer, each node is fully connected to every node in subsequent layer. For each edge, a separate, trainable activation function is applied. At each node, only a summation operation is performed over all incoming edges. As shown in the bottom right corner of Fig. 1, learnable activation functions are defined as weighted sums of B-splines, denoted by the B-spline basis functions  $B_i$ , with the fixed residual function chosen as Sigmoid Linear Unit (SiLU):

$$\text{KAN}(x) = w_1 \cdot \text{SiLU}(x) + w_2 \cdot \sum_{i=0}^{G+k-1} c_i \cdot B_i(x). \quad (2)$$

The weights  $w_1$ ,  $w_2$  and the basis function coefficients  $c_i$  are trainable parameters of spline. The basis function  $B_i$  is chosen as a  $k$ -th degree polynomial, with the default value  $k = 3$ . The grid parameter  $G$  determines the degree of B-spline construction with the default value  $G = 5$ . In detail, for specified parameters  $k$ ,  $G$  and the domain  $[t_0, t_G]$ , a vector of equidistant knot points  $\vec{t} = (t_{-k}, \dots, t_0, \dots, t_{G+k})$  is constructed. Subsequently,  $G + k$  basis functions  $B_i^k(x)$  are defined recursively as follows:

$$B_i^0(x) = \begin{cases} 1 & \text{if } t_i \leq x < t_{i+1}, \\ 0 & \text{otherwise,} \end{cases} \quad (3)$$

and for  $k > 0$ :

$$B_i^k(x) = \frac{x - t_i}{t_{i+k} - t_i} B_i^{k-1}(x) + \frac{t_{i+k+1} - x}{t_{i+k+1} - t_{i+1}} B_{i+1}^{k-1}(x). \quad (4)$$

By further allowing coefficient  $c_i$  to locally adapt and alter the entire spline, KAN can fit arbitrary mapping functions without a specific form.

## KAN-Fusion

Intuitively, spline functions allow for more direct adjustment of the importance weight of spectral sequence and spatial texture features, and the shallow design essentially avoids the COD. Based on this concept, we utilize a combination of triangular KAN layers for the fusion of LR-HSI and HR-MSI, with details as follows.

To facilitate the linear transformation by the KAN layer, we first fold the input HR-MSI  $\mathbf{X}$  and the upsampled LR-HSI  $UP(\mathbf{Y})$  in the spatial dimension:

$$\mathbf{X}_0 = \text{reshape}(\mathbf{X}), \quad \mathbf{X}_0 \in \mathbb{R}^{HW \times C} \quad (5)$$

$$\mathbf{Y}_0 = \text{reshape}(UP(\mathbf{Y})), \quad \mathbf{Y}_0 \in \mathbb{R}^{HW \times C} \quad (6)$$

Next, as 7,  $\mathbf{X}_0$  and  $\mathbf{Y}_0$  are individually mapped to a common dimension  $D$  by a KAN layer,  $D$  is set to 256 as a hyperparameter. Subsequently, a KAN layer aligns two concatenated vectors while maintaining the channel dimension as  $D$ . For ease of handling, we reshape the output

$O_0 \in \mathbb{R}^{HW \times D}$  into a feature map of dimensions  $O_0' \in \mathbb{R}^{D \times H \times W}$ .

$$\mathbf{O}_0 = \text{KAN}(\text{concat}[\text{KAN}(\mathbf{X}_0), \text{KAN}(\mathbf{Y}_0)]) \quad (7)$$

$$\mathbf{O}_0' = \text{reshape}(\mathbf{O}_0) \quad \mathbf{O}_0 \in \mathbb{R}^{D \times H \times W} \quad (8)$$

Finally, the fused feature  $\mathbf{O}_0'$  is passed through the KAN-CAB module for feature extraction.

### KAN Channel Attention Block (KAN-CAB)

HSR-KAN adopts  $L$  consecutive KAN-CAB modules for spectral feature extraction. KAN-CAB module consists of an SENet structure composed of two KAN layers. Details are as follows.

KAN-CAB can be mainly divided into two stages as Listing 1. In first stage, *Global Average Pooling* (GAP) is applied to compress the feature of each spectral channel in input feature map (e.g., for the feature map  $O_i$  of the  $i$ -th layer). This means that for each spectral channel, we obtain a single value to represent its global importance. In the second stage, two consecutive KAN layers are utilized to learn importance weights of each channel. These weights are then used to generate a vector that reweights channels of the input feature map. Finally, we multiply the spectral channel weight vector with input  $O_i$  channel-wise, precisely adjusting the global composition ratio of local spectral pixels.

Employing a channel attention module integrated with KAN, rather than simply stacking KAN layers, effectively circumvents the COD. It is noteworthy that although the KAN layer incorporates an MLP, the initial intent of integrating the MLP is to concurrently learn the composite structure (extrinsic degrees of freedom) and univariate functions (intrinsic degrees of freedom). In essence, the KAN layer is proposed as an effective linear model. Corresponding to the HSI-SR task, the extraction of spatial structural information is equally crucial. Therefore, designing a module based on the spectral channel attention mechanism is a viable option. Such a module adeptly balances the extraction of spatial texture features with the modeling of spectral sequence information. After extracting feature using  $L$  layers of KAN-CAB, resulting in the output  $O_l$ , it is then input into the Restructure module to reshape it into the spatial shape of HR-HSI.

### Restructure Module and Loss Function

Restructure module is used to restore the spatial shape of HR-HSI, the Restructure module is represented as follows:

$$\bar{\mathbf{Z}} = \text{Conv}(\text{ReLU}(\text{Conv}(O_l))) + \text{UP}(\mathbf{Y}), \quad (9)$$

here,  $O_l$  denotes the output after feature extraction by  $L$  layers of KAN-CAB.  $\bar{\mathbf{Z}}$  represents the predicted HR-HSI. Conv denotes a convolution operation with a kernel size of 3, while ReLU denotes the activation function.

Intuitively, the introduction of spline functions indeed provides the model with a more refined adjustment capability. However, the risk of overfitting that may arise from fully connected KAN layers cannot be overlooked. Employing sparse spline functions is an effective strategy to address this challenge. It should be noted that what needs to

listing 1: PyTorch style code for KAN-CAB

```

class KAN_SA(nn.Module):
    def __init__(self, dim):
        self.dim = dim
        self.kan1 = KAN(dim, dim)
        self.kan2 = KAN(dim, dim)

    def forward(self, x):
        b, c, h, w = x.shape
        assert c == self.dim
        shortcut = x
        # b c h w -> b c 1 1
        score = F.adaptive_avg_pool2d(x, (1, 1))
        score = score.reshape((b, c))
        score = self.kan1(score)
        score = self.kan2(score)
        score = score.reshape((b, c, 1, 1))
        # channel-wise multiplication
        x = x * score
        return x + shortcut

```

be sparsed is not the weights, but the spline functions.

$$\ell_{\text{total}} = |\bar{\mathbf{Z}} - \mathbf{Z}|_1 + \ell_{\text{sparse}}, \quad (10)$$

Here,  $\ell_{\text{sparse}}$  represents the default activation sparsity loss in (Liu et al. 2024) (See Appendix A for detail definition).

## Experiment

### Datasets and Benchmark

We use three public datasets for testing: CAVE (Yasuma et al. 2010), Harvard (Chakrabarti and Zickler 2011) and Chikusei (Yokoya and Iwasaki 2016). Specifically, the CAVE dataset consists of 32 scenes, each with a spatial dimension of  $512 \times 512$ , and includes 31 spectral bands. We select 20 images for training and 11 images for testing. The Harvard database has 50 indoor and outdoor images captured under daylight conditions, along with 27 indoor images taken under artificial and mixed lighting. Each HSI in this database has a spatial size of  $1392 \times 1040$  pixels and contains 31 spectral bands. We crop the top-left part of each image ( $1000 \times 1000$  pixels) and randomly select 10 images for testing. Chikusei is a remote sensing HSI with  $2048 \times 2048$  spatial pixels and 128 spectral channels. The upper-left corner of  $1024 \times 2048$  pixels is used for training data, while the remaining area is divided into 8 patches of  $512 \times 512$  pixels each for testing.

The comparative methods include the traditional method: FUSE (Wei, Dobigeon, and Tournet 2015). CNN-based methods include SSRNet (Zhang et al. 2021), MHFNet (Xie et al. 2022), and HSRnet (Hu et al. 2022). Transformer-based methods include Fusformer (Hu, Huang, and Deng 2021), DCTransformer (Ma et al. 2024), and HSR-Diff (Wu et al. 2023), with HSR-Diff being based on diffusion methods. The selected image generation quality metrics include PSNR, SSIM, SAM, and ERGAS.

### Implementation Details

We use the PyTorch framework with code implementation and training on Nvidia A800 GPUs. The *batch size* is set to

Method	Scale	CAVE				Harvard				Chikusei			
		PSNR	SAM	ERGAS	SSIM	PSNR	SAM	ERGAS	SSIM	PSNR	SAM	ERGAS	SSIM
FUSE	$\times 2$	50.81	3.34	2.69	0.989	51.04	2.31	2.28	0.992	32.81	3.09	4.96	0.931
MHF-Net	$\times 2$	52.04	2.86	1.27	0.995	43.20	4.02	12.11	0.981	37.19	2.86	4.52	0.957
HSRnet	$\times 2$	52.89	2.33	1.10	0.996	50.29	2.43	2.34	0.989	39.95	1.86	3.07	0.968
Fusformer	$\times 2$	53.03	2.26	1.07	0.996	51.07	2.34	2.28	0.992	41.26	1.69	2.77	0.970
DCTransformer	$\times 2$	53.74	2.07	0.97	0.998	51.61	2.29	2.24	0.994	41.87	1.53	2.68	0.972
HSR-Diff	$\times 2$	<u>53.98</u>	<u>1.94</u>	<u>0.90</u>	<u>0.999</u>	<u>51.68</u>	<u>2.16</u>	<u>2.13</u>	<u>0.996</u>	<u>42.12</u>	<u>1.48</u>	<u>2.54</u>	<u>0.978</u>
HSR-KAN	$\times 2$	<b>54.62</b>	<b>1.86</b>	<b>0.79</b>	<b>0.999</b>	<b>51.81</b>	<b>2.10</b>	<b>1.86</b>	<b>0.997</b>	<b>42.31</b>	<b>1.37</b>	<b>2.48</b>	<b>0.981</b>
FUSE	$\times 4$	39.72	4.83	4.18	0.975	42.06	3.23	3.14	0.977	27.76	4.80	7.22	0.882
MHF-Net	$\times 4$	46.32	3.33	1.74	0.992	40.37	4.64	24.17	0.966	33.19	3.18	6.24	0.927
HSRnet	$\times 4$	47.82	2.66	1.34	0.995	44.29	2.66	2.45	0.984	36.95	2.08	3.60	0.952
Fusformer	$\times 4$	48.56	2.52	1.30	0.995	45.06	2.62	2.39	0.987	37.01	2.04	3.54	0.958
DCTransformer	$\times 4$	48.78	2.49	1.29	0.996	46.34	2.59	2.36	0.989	37.12	2.01	3.46	0.961
HSR-Diff	$\times 4$	<u>48.86</u>	<u>2.42</u>	<u>1.27</u>	<u>0.996</u>	<u>46.52</u>	<u>2.54</u>	<u>2.32</u>	<u>0.991</u>	<u>37.19</u>	<u>1.98</u>	<u>3.42</u>	<u>0.964</u>
HSR-KAN	$\times 4$	<b>49.17</b>	<b>2.40</b>	<b>1.25</b>	<b>0.997</b>	<b>47.12</b>	<b>2.48</b>	<b>2.29</b>	<b>0.993</b>	<b>37.42</b>	<b>1.87</b>	<b>3.31</b>	<b>0.968</b>
FUSE	$\times 8$	36.24	8.64	6.49	0.818	40.13	4.05	3.98	0.980	26.81	6.21	10.04	0.869
MHF-Net	$\times 8$	41.17	4.54	2.95	0.837	34.86	10.99	30.17	0.916	29.21	4.02	8.09	0.911
Fusformer	$\times 8$	43.21	3.89	2.41	0.869	40.96	4.24	3.99	0.976	33.96	2.86	4.45	0.939
DCTransformer	$\times 8$	44.49	<u>3.19</u>	<u>2.08</u>	0.898	41.86	3.89	3.15	0.980	34.08	2.54	4.02	0.945
HSR-Diff	$\times 8$	<u>44.54</u>	3.23	2.13	<u>0.899</u>	<u>41.91</u>	<u>3.44</u>	<u>3.12</u>	<u>0.982</u>	<u>34.21</u>	<u>2.31</u>	<u>3.86</u>	<u>0.949</u>
HSR-KAN	$\times 8$	<b>44.89</b>	<b>3.17</b>	<b>2.04</b>	<b>0.991</b>	<b>42.14</b>	<b>3.40</b>	<b>3.09</b>	<b>0.984</b>	<b>34.51</b>	<b>2.23</b>	<b>3.64</b>	<b>0.951</b>
Best Value	-	$+\infty$	0	0	1	$+\infty$	0	0	1	$+\infty$	0	0	1

Table 1: Quantitative comparisons of different approaches were conducted on the CAVE, Harvard, and Chikusei test datasets. The best results are highlighted in **bold**, while the second-best results are underlined.

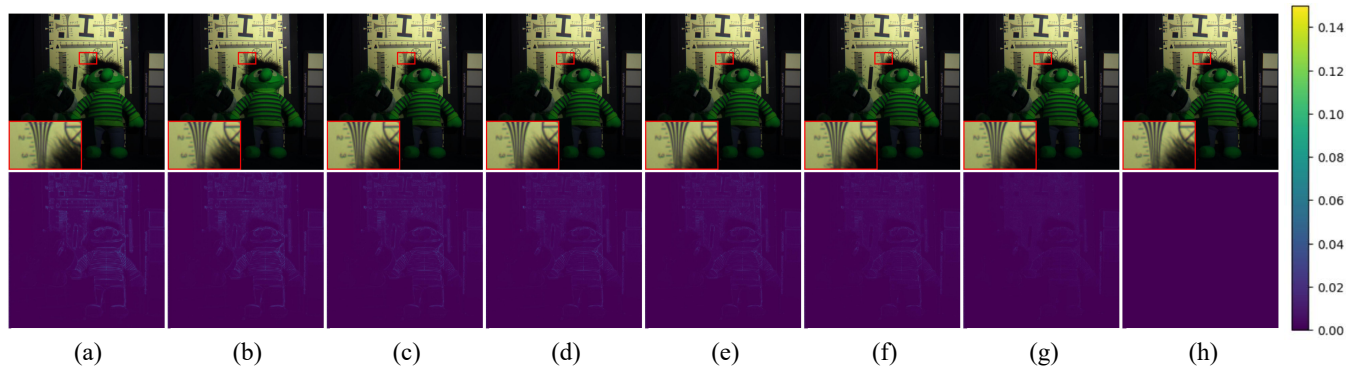


Figure 2: Visual quality comparison on the CAVE for  $\times 4$  SR, where the first row shows pseudo-color (R-20, G-30, B-2) images and second row shows corresponding heatmaps (mean squared error). (a) FUSE, (b) MHF-Net, (c) HSRnet, (d) Fusformer, (e) DCTransformer, (f) HSR-Diff, (g) HSR-KAN, (h) GT.

32. We use the *Adam* optimizer with an initial learning rate of  $4 \times 10^{-4}$ . The learning rate is decayed by a factor of 0.1 every 100 epochs. All methods are trained for 1000 epochs.

For ease of comparison, we set the number of KAN-CAB layers  $L$  to 4. All comparison methods follow the default settings in respective papers or open-source codes. We utilize the *efficient-kan*<sup>1</sup> library to implement the KAN layer. For fair comparison, we evaluate the computational efficiency and model size of all models on *fvcore*<sup>2</sup>.

<sup>1</sup><https://github.com/Blealtan/efficient-kan>

<sup>2</sup><https://github.com/facebookresearch/fvcore>

Ground Truth (GT) patches are cropped to  $64 \times 64$ , and then downsampled to  $16 \times 16$  to serve as LR-HSI patches. The LR-HSI patches are generated from the GT patches by applying a Gaussian blur with a kernel size of  $3 \times 3$  and a standard deviation of 0.5. In addition, the spectral response function of the Nikon D700 camera (Dian, Li, and Kang 2021) is used to generate HR-MSI patches.

### Comparison with State of Arts Methods

**Results on CAVE.** Table 1 presents the average image generation quality of 11 test images at  $\times 2$ ,  $\times 4$ ,  $\times 8$  scaling. HSR-KAN achieves best results in all quantitative met-

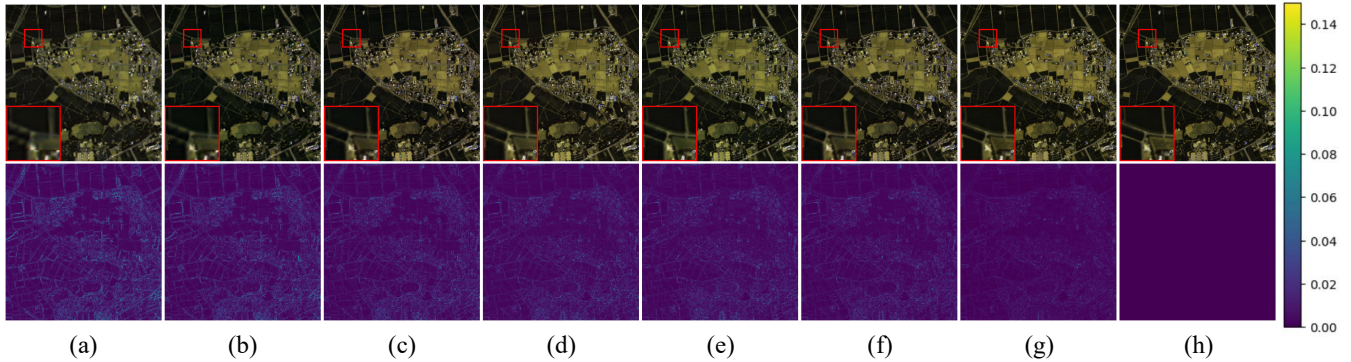


Figure 3: Visual quality comparison on Chikusei for  $\times 4$  SR, where first row shows pseudo-color (R-64, G-58, B-16) images and second row shows corresponding heatmaps. (a) FUSE, (b) MHF-Net, (c) HSRnet, (d) Fusformer, (e) DCTransformer, (f) HSR-Diff, (g) HSR-KAN, (h) GT.

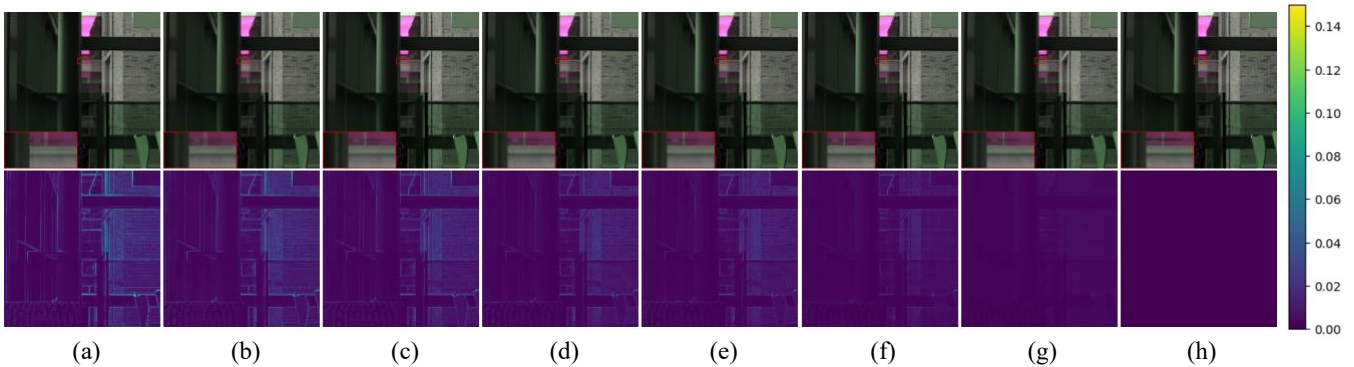


Figure 4: Visual quality comparison on Harvard for  $\times 4$  SR, where first row shows the pseudo-color (R-29, G-22, B-31) images and second row shows corresponding heatmaps. (a) FUSE, (b) MHF-Net, (c) HSRnet, (d) Fusformer, (e) DCTransformer, (f) HSR-Diff, (g) HSR-KAN, (h) GT.

rics. Furthermore, in Fig. 2, we display pseudo-colored images for scaling factor  $\times 4$  of *charts and stuffed toys* generated by various models, along with their corresponding Mean Squared Error (MSE) heatmaps. These visual results indicate that all compared methods produce satisfactory outcomes. Notably, the HSR-KAN model performs most excellently, with the smallest MSE relative to the GT.

**Results on Chikusei.** Table 1 illustrates the average image generation quality metrics for eight test patches from the Chikusei dataset at  $\times 2$ ,  $\times 4$ , and  $\times 8$  scaling. HSR-KAN model exhibits significant enhancements across all evaluated metrics. Fig. 3 display pseudo-color images for  $\times 4$  SR generated by comparative models, accompanied by their respective MSE heatmaps. While all methods yield satisfactory visual outcomes, displayed heatmaps suggest that the image produced by our approach are more closely aligned with GT. These results show that HSR-KAN model is also effective to remote sensing HSIs.

**Generalization Performance on Harvard.** To validate the generalization performance of HSR-KAN, we test mod-

els trained on the CAVE dataset on the Harvard dataset *without any additional training or fine-tuning*. We present the average image generation quality for all images in the Harvard dataset in Table 4 of  $\times 2$ ,  $\times 4$  and  $\times 8$  scaling. Fig. 4 shows the pseudo-color super-resolution images for  $\times 4$  SR generated by various models on the Harvard dataset, along with their corresponding heatmaps. HSR-KAN demonstrates the best visual performance, without introducing additional noise or artifacts. Quantitative experimental results and image generation results show that HSR-KAN achieves the best generalization performance.

In summary, HSR-KAN not only achieves exceptional performance in both quantitative and qualitative analyses, surpassing SOTA methods, but it also demonstrates excellent generalization performance (Supplementary validation experiments, please see Appendix B).

### Ablation Study

To gain more insights into our model, we conduct a set of ablative experimentson on the CAVE dataset for  $\times 4$  SR. The performance of various ablation models is presented in Table

Ablation	Variant	#Params(M)	#FLOPs(G)	PSNR
Baseline	-	7.30	7.87	49.17
Cores	Conv	6.78	27.19	41.34
	MLP	2.59	7.86	36.81
	Self-Attention	4.16	7.87	42.87
Fusion	Stack Fusion	5.98	3.04	46.02
Loss	without $\ell_{\text{sparse}}$	7.30	7.87	47.28
Attention	without CAB	7.30	27.19	41.03

Table 2: Ablation quantitative results for HSR-KAN on CAVE datasets for  $\times 4$  SR. #Params means the number of network parameters. #FLOPs denotes the number of FLOPs.

2, with detailed ablative implementation as follows.

**Impact of KAN Layer.** To validate the importance of incorporating the KAN layer, we replace the KAN layer with other popular computational cores. As shown in the first three rows of Table 2, replacing the KAN layer with an MLP, CNN, and Self-attention module does not achieve better performance.

**Impact of KAN-Fusion.** KAN-Fusion as a KAN-based fusion module, is compared with *Stack Fusion* (the LR-HSI is simply upsampled and concatenated with HR-HSI) used by Fusformer and HSR-Diff. Experimental results, as shown in the fourth row of Table 2. Results show that the PSNR of Stack Fusion-based model is far less than that of KAN-Fusion-based baseline model.

**Impact of Sparse Loss.** The introduction of B-spline functions achieves finer granularity in weight adjustment, but it also tends to lead to overfitting. Therefore, the introduction of a regularized sparsity loss function is particularly necessary. To quantitatively analyze the effect of the sparsity loss function, we compare the performance of models with and without it, with the comparative results listed in the fifth row of Table 2. The variation in loss and PSNR values in Fig. 5. These experimental results indicate that during the training process, initial convergence rate is faster without using a sparsity loss function, but as the model training progresses, the convergence rate significantly lags behind that of the training using a sparsity loss function. Overall, training HSR-KAN with a sparsity loss function can significantly enhance the upper limit of network performance.

**Impact of Channel Attention Block.** Intuitively, integrating a channel attention mechanism with KAN can effectively mitigate the COD. To quantitatively analyze the impact of the KAN-CAB, we compare KAN-CAB with a network that simply stacks KAN layers (as indicated as 'Without CAB' in Table 2). Experimental results demonstrate that the KAN-CAB, while ensuring a reduction in computational load, achieves a significant enhancement in performance, and as shown in Fig. 5, substantially improves the convergence rate of network. In summary, KAN-CAB does indeed effectively reduce the impact of the COD.

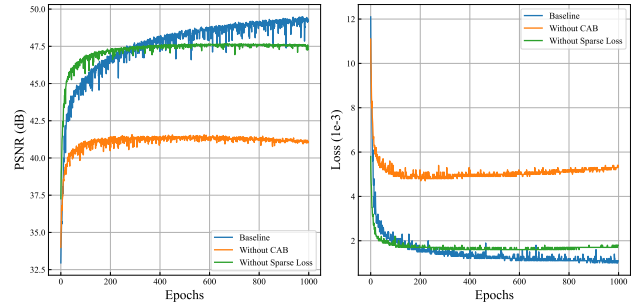


Figure 5: The full-size HSR-KAN model (Baseline), is compared with the two ablation models 'Without Sparse Loss' and 'Without CAB' for their training performance on the CAVE dataset for  $\times 4$  SR. The left graph plots the variation in PSNR values, while the right graph shows the changes in loss values.

Method	#Params(M)	#FLOPs(G)	Time(ms)	PSNR
MFH-Net	0.79	2.53	22.05	46.32
HSRnet	1.90	2.02	3.12	47.82
Fusformer	0.50	10.12	4.40	48.56
DCTransformer	8.12	76.79	200.74	48.78
HSR-Diff	10.14	140.15	16.14	48.86
HSR-KAN	7.30	7.87	6.18	49.17

Table 3: Quantitative comparisons of computational performance on the CAVE dataset for  $\times 4$  SR. #Params means the number of network parameters. #FLOPs denotes the number of FLOPs.

## Comparison of Efficiency

To verify the feasibility of model deployment, we perform a basic evaluation of inference performance. We test on the CAVE dataset with a batch size set to 1 for  $\times 4$  SR. Experimental quantitative results are shown in Table 3. Compared to advanced SR methods HSR-Diff, which is based on diffusion, and DCTransformer, which is based on Transformer, our model significantly reduces model size and inference time by sparsity of spline function computations and lightweight network structure design.

## Conclusion

We propose an innovative hybrid neural network for fusing a LR-HSI and a HR-MSI to generate a HR-HSI, called HSR-KAN, which harnesses the collective advantages of KANs, CNNs, and MLPs. Specifically, HSR-KAN achieves finer-grained modeling capability through the integration of KANs, while effectively addressing the issue of the KAN network being susceptible to the COD in deep fully connected structures by combining it with MLP and CNN. HSR-KAN demonstrates exceptional SR performance while maintaining a fewer model parameter and computational burden. Extensive experiments prove that HSR-KAN surpasses existing state-of-the-art (SOAT) methods while maintaining high computational efficiency.

## References

- Akhtar, N.; Shafait, F.; and Mian, A. 2015. Bayesian sparse representation for hyperspectral image super resolution. In *2015 IEEE Conference on Computer Vision and Pattern Recognition (CVPR)*.
- Borsoi, R.; Imbiriba, T.; and Bermudez, J. 2018. Super-Resolution for Hyperspectral and Multispectral Image Fusion Accounting for Seasonal Spectral Variability. *Cornell University - arXiv, Cornell University - arXiv*.
- Chakrabarti, A.; and Zickler, T. 2011. Statistics of real-world hyperspectral images. In *CVPR 2011*, 193–200. IEEE.
- Chen, N.; Yue, J.; Fang, L.; and Xia, S. 2023. SpectralDiff: A Generative Framework for Hyperspectral Image Classification With Diffusion Models. *IEEE Transactions on Geoscience and Remote Sensing*, 61: 1–16.
- Cheon, M. 2024. Demonstrating the Efficacy of Kolmogorov-Arnold Networks in Vision Tasks. arXiv:2406.14916.
- Dian, R.; Li, S.; and Kang, X. 2021. Regularizing Hyperspectral and Multispectral Image Fusion by CNN Denoiser. *IEEE Transactions on Neural Networks and Learning Systems*, 1124–1135.
- Dong, C.; Loy, C. C.; He, K.; and Tang, X. 2016. Image Super-Resolution Using Deep Convolutional Networks. *IEEE Transactions on Pattern Analysis and Machine Intelligence*, 295–307.
- Donoho, D. L.; et al. 2000. High-dimensional data analysis: The curses and blessings of dimensionality. *AMS math challenges lecture*, 1(2000): 32.
- Genet, R.; and Inzirillo, H. 2024. TKAN: Temporal Kolmogorov-Arnold Networks. arXiv:2405.07344.
- Goodfellow, I.; Pouget-Abadie, J.; Mirza, M.; Xu, B.; Warde-Farley, D.; Ozair, S.; Courville, A.; and Bengio, Y. 2020. Generative adversarial networks. *Communications of the ACM*, 63(11): 139–144.
- Ho, J.; Jain, A.; and Abbeel, P. 2020. Denoising diffusion probabilistic models. *Advances in neural information processing systems*, 33: 6840–6851.
- Hu, J.; Shen, L.; Albanie, S.; Sun, G.; and Wu, E. 2019. Squeeze-and-Excitation Networks. arXiv:1709.01507.
- Hu, J.-F.; Huang, T.-Z.; and Deng, L.-J. 2021. Fusformer: A Transformer-based Fusion Approach for Hyperspectral Image Super-resolution. *Cornell University - arXiv, Cornell University - arXiv*.
- Hu, J.-F.; Huang, T.-Z.; Deng, L.-J.; Jiang, T.-X.; Vivone, G.; and Chanussot, J. 2022. Hyperspectral Image Super-Resolution via Deep Spatospectral Attention Convolutional Neural Networks. *IEEE Transactions on Neural Networks and Learning Systems*, 7251–7265.
- Islam, M. A.; Xing, W.; Zhou, J.; Gao, Y.; and Paliwal, K. K. 2024. Hy-Tracker: A Novel Framework for Enhancing Efficiency and Accuracy of Object Tracking in Hyperspectral Videos. *IEEE Transactions on Geoscience and Remote Sensing*, 62: 1–14.
- Kolmogorov, A. N. 1957. On the representation of continuous functions of many variables by superposition of continuous functions of one variable and addition. In *Doklady Akademii Nauk*, volume 114, 953–956. Russian Academy of Sciences.
- Köppen, M. 2002. On the training of a Kolmogorov Network. In *Artificial Neural Networks—ICANN 2002: International Conference Madrid, Spain, August 28–30, 2002 Proceedings 12*, 474–479. Springer.
- Ledig, C.; Theis, L.; Huszar, F.; Caballero, J.; Cunningham, A.; Acosta, A.; Aitken, A.; Tejani, A.; Totz, J.; Wang, Z.; and Shi, W. 2017. Photo-Realistic Single Image Super-Resolution Using a Generative Adversarial Network. In *2017 IEEE Conference on Computer Vision and Pattern Recognition (CVPR)*.
- Li, C.; Liu, X.; Li, W.; Wang, C.; Liu, H.; and Yuan, Y. 2024. U-KAN Makes Strong Backbone for Medical Image Segmentation and Generation. arXiv:2406.02918.
- Li, S.; Dian, R.; Fang, L.; and Bioucas-Dias, J. M. 2018. Fusing Hyperspectral and Multispectral Images via Coupled Sparse Tensor Factorization. *IEEE Transactions on Image Processing*, 4118–4130.
- Liu, Z.; Wang, Y.; Vaidya, S.; Ruehle, F.; Halverson, J.; Soljačić, M.; Hou, T. Y.; and Tegmark, M. 2024. KAN: Kolmogorov-Arnold Networks. arXiv:2404.19756.
- Ma, Q.; Jiang, J.; Liu, X.; and Ma, J. 2024. Reciprocal transformer for hyperspectral and multispectral image fusion. *Information Fusion*, 104: 102148.
- Ren, T.; Shen, Q.; Fu, Y.; and You, S. 2024. Point-Supervised Semantic Segmentation of Natural Scenes via Hyperspectral Imaging. In *Proceedings of the IEEE/CVF Conference on Computer Vision and Pattern Recognition (CVPR) Workshops*, 1357–1367.
- Sprecher, D. A.; and Draghici, S. 2002. Space-filling curves and Kolmogorov superposition-based neural networks. *Neural Networks*, 57–67.
- Tikhomirov, V. M. 1991. *On the Representation of Continuous Functions of Several Variables as Superpositions of Continuous Functions of a Smaller Number of Variables*, 378–382.
- Vaswani, A.; Shazeer, N.; Parmar, N.; Uszkoreit, J.; Jones, L.; Gomez, A.; Kaiser, L.; and Polosukhin, I. 2017. Attention is All you Need. *Neural Information Processing Systems, Neural Information Processing Systems*.
- Wei, Q.; Bioucas-Dias, J.; Dobigeon, N.; and Tourneret, J.-Y. 2014. Hyperspectral and Multispectral Image Fusion based on a Sparse Representation. *IEEE Transactions on Geoscience and Remote Sensing, IEEE Transactions on Geoscience and Remote Sensing*.
- Wei, Q.; Dobigeon, N.; and Tourneret, J.-Y. 2015. Fast Fusion of Multi-Band Images Based on Solving a Sylvester Equation. *IEEE Transactions on Image Processing*, 4109–4121.
- Wu, C.; Wang, D.; Bai, Y.; Mao, H.; Li, Y.; and Shen, Q. 2023. HSR-Diff: Hyperspectral image super-resolution via conditional diffusion models. In *Proceedings of the*



*IEEE/CVF International Conference on Computer Vision*, 7083–7093.

Xie, Q.; Zhou, M.; Zhao, Q.; Xu, Z.; and Meng, D. 2022. MHF-Net: An Interpretable Deep Network for Multispectral and Hyperspectral Image Fusion. *IEEE Transactions on Pattern Analysis and Machine Intelligence*, 1457–1473.

Yasuma, F.; Mitsunaga, T.; Iso, D.; and Nayar, S. K. 2010. Generalized Assorted Pixel Camera: Postcapture Control of Resolution, Dynamic Range, and Spectrum. *IEEE Transactions on Image Processing*, 2241–2253.

Yokoya, N.; and Iwasaki, A. 2016. Airborne hyperspectral data over Chikusei. *Space Appl. Lab., Univ. Tokyo, Tokyo, Japan, Tech. Rep. SAL-2016-05-27*, 5(5): 5.

Zhang, X.; Huang, W.; Wang, Q.; and Li, X. 2021. SSR-NET: Spatial–Spectral Reconstruction Network for Hyperspectral and Multispectral Image Fusion. *IEEE Transactions on Geoscience and Remote Sensing*, 5953–5965.

## Appendix

### A. Spline Sparsity Loss Function.

We define the L1 norm of each spline activation function  $\phi$  in HSR-KAN as the average magnitude across its  $N_p$  inputs, given by:

$$|\phi|_1 \equiv \frac{1}{N_p} \sum_{s=1}^{N_p} |\phi(x^{(s)})|. \quad (11)$$

For a KAN layer  $\Phi$  with  $n_{\text{in}}$  inputs and  $n_{\text{out}}$  outputs, the L1 norm of  $\Phi$  is defined as the sum of the L1 norms of all constituent activation functions:

$$|\Phi|_1 \equiv \sum_{i=1}^{n_{\text{in}}} \sum_{j=1}^{n_{\text{out}}} |\phi_{i,j}|_1. \quad (12)$$

Furthermore, the entropy of  $\Phi$  is defined as:

$$S(\Phi) \equiv - \sum_{i=1}^{n_{\text{in}}} \sum_{j=1}^{n_{\text{out}}} \frac{|\phi_{i,j}|_1}{|\Phi|_1} \log \left( \frac{|\phi_{i,j}|_1}{|\Phi|_1} \right). \quad (13)$$

The total training objective  $\ell$  is composed of the prediction loss  $|\bar{\mathbf{Z}} - \mathbf{Z}|_1$ , plus L1 and entropy regularization terms for all KAN layers, expressed as:

$$\ell = |\bar{\mathbf{Z}} - \mathbf{Z}|_1 + \lambda \left( \mu_1 \sum_{l=0}^{L-1} |\Phi_l|_1 + \mu_2 \sum_{l=0}^{L-1} S(\Phi_l) \right), \quad (14)$$

where  $\mu_1$  and  $\mu_2$  are coefficients that are typically set equal to 1, and  $\lambda$  is the hyperparameter that governs the overall strength of regularization is also set to 1 in HSR-KAN.

### B. Supplementary Validation Experiment.

**subsubsectionImpact of Spline Order.** To explore the impact of *Spline Order* on network performance, we compare the network’s performance under different *Spline Order* settings (with *Grid Size* kept at 5). From the results in Table 4, we can observe that as the *Spline Order* increases, the size of the network model grows linearly while the FLOPs remain constant. However, when the *Spline Order* exceeds 3, the SR performance of the network does not improve proportionally with the increase in model size. With a *Spline Order* of 3, HSR-KAN achieves the optimal balance between SR performance and computational efficiency.

Spline Order	#Params(M)	#FLOPs(G)	PSNR	SSIM
1	6.25	7.87	39.12	0.975
3	7.30	7.87	49.17	0.997
5	8.35	7.87	49.20	0.997
7	9.40	7.87	49.23	0.997
9	10.45	7.87	48.18	0.996

Table 4: Quantitative comparison results regarding different *Spline Order* (with *Grid Size* kept at 5). #Params means the number of network parameters. #FLOPs denotes the number of FLOPs.

**Impact of Grid Size.** Different spline *Grid Size* indicates the internal adjustment range of the learnable activation function. We further explore the impact of this parameter setting on the SR performance of HSR-KAN (with *Spline Order* kept at 3). As shown in Table 5, when the *Grid Size* increases linearly, the model size also grows linearly, while the FLOPs remain unchanged. However, when the *Grid Size* exceeds 5, there is no significant improvement in SR performance. Therefore, a *Grid Size* of 5 represents the optimal balance point.

Grid Size	#Params(M)	#FLOPs(G)	PSNR	SSIM
1	5.21	7.87	36.28	0.812
3	6.25	7.87	40.28	0.843
5	7.30	7.87	49.17	0.997
7	8.35	7.87	49.02	0.997
9	9.40	7.87	48.71	0.996

Table 5: Quantitative comparison results regarding different *Grid Size* (with *Spline Order* kept at 3). #Params means the number of network parameters. #FLOPs denotes the number of FLOPs.